THE JOURNAL OF PHYSICAL CHEMISTRY C
A JOURNAL OF THE AMERICAN CHEMICAL SOCIETY

pubs.acs.org/JPCC

Article

High-Pressure Properties of Wolframite-Type $ScNbO_4$

Tarik Ouahrani,* Alka B. Garg, Rekha Rao, Placida Rodríguez-Hernández, Alfonso Muñoz, Michael Badawi, and Daniel Errandonea*

Cite This: *J. Phys. Chem. C* 2022, 126, 4664−4676

Read Online

ACCESS | Metrics & More | Article Recommendations | Supporting Information

ABSTRACT: In this work, we used Raman spectroscopic and optical absorption measurements and first-principles calculations to unravel the properties of wolframite-type $ScNbO_4$ at ambient pressure and under high pressure. We found that monoclinic wolframite-type $ScNbO_4$ is less compressible than most wolframites and that under high pressure it undergoes two phase transitions at ∼5 and ∼11 GPa, respectively. The first transition induces a 9% collapse of volume and a 1.5 eV decrease of the band gap energy, changing the direct band gap to an indirect one. According to calculations, pressure induces symmetry changes ($P2/c$−$Pnna$−$P2/c$). The structural sequence is validated by the agreement between phonon calculations and Raman experiments and between band structure calculations and optical absorption experiments. We also obtained the pressure dependence of Raman modes and proposed a mode assignment based upon calculations. They also provided information on infrared modes and elastic constants. Finally, noncovalent and charge analyses were employed to analyze the bonding evolution of $ScNbO_4$ under pressure. They show that the bonding nature of $ScNbO_4$ does not change significantly under pressure. In particular, the ionicity of the wolframite phase is 61% and changes to 63.5% at the phase transition taking place at ∼5 GPa.

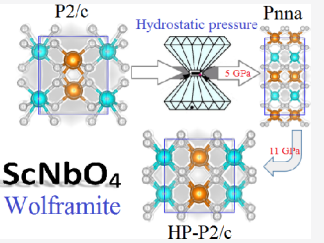

INTRODUCTION

During the past decade, ternary MTO_4 oxides have attracted great interest from both fundamental and applied research.[1−4] However, understanding of their responses to the application of pressure and other external fields is not fully known. Fundamental research is motivated by the need to systematically understand the properties of these compounds and their relationship with chemical bonding.[1−4] On the other hand, from the application point of view, many studies are driven by the multiple technological applications of MTO_4 oxides, which range from photocatalytic applications to uses as laser host and scintillating materials.[1−4] Among MTO_4 oxides, one of the most interesting groups is formed by wolframite-type compounds.[5] These ternary oxides are isomorphic to natural iron manganese tungstate, the mineral wolframite. The crystal structure of wolframite-type oxides belongs to the monoclinic space group $P2/c$.[6] A schematic representation of the structure is shown in the inset of Figure 1. In the structural framework, the M cations are bonded to six oxygen atoms to form distorted MO_6 octahedral units that share corners with six equivalent TO_6 octahedral units and edges with two equivalent MO_6 octahedra. The oxygen atoms form a nearly hexagonal-close-packed network.

Most wolframite oxides are either tungstates or molybdates. However, in the Inorganic Crystal Structure Database,[7] there are two niobates reported: $InNbO_4$[8] and $ScNbO_4$.[9] The first compound has been studied due to its photocatalytic properties and because it can be used as a phosphor for light-emitting sources.[10] $ScNbO_4$ has received attention very recently because of its luminescent properties.[11] It is also a material of relevance for earth sciences. It has been found in

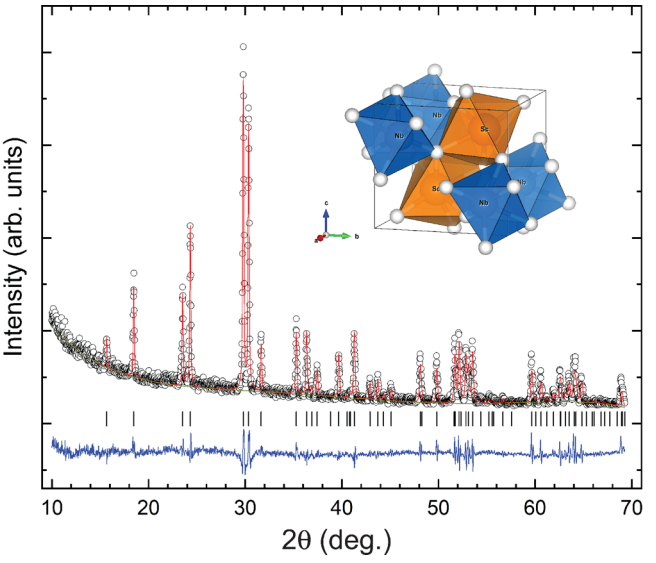

Figure 1. Powder X-ray diffraction pattern of $ScNbO_4$ (circles). The Rietveld refinement is shown in red, and the residuals are shown in blue. Tick marks are the positions of calculated peaks. The inset shows the crystal structure of $ScNbO_4$. ScO_6 and NbO_6 octahedra are shown in orange and blue, respectively. The white circles represent the oxygen atoms.

Received: December 11, 2021
Revised: February 14, 2022
Published: February 23, 2022

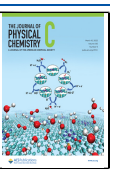

granitic pegmatites in different terrestrial regions.[12] The high-pressure (HP) behavior of $InNbO_4$ has been studied,[13] but the HP behavior of $ScNbO_4$ has not. Combined X-ray diffraction, Raman spectroscopic, and density functional theory studies performed on $InNbO_4$ have discovered a pressure-induced transition at 10.8 GPa.[13] The phase transition is first order in nature, preserving the space-group symmetry; i.e., the HP phase is also described by space group $P2/c$. In addition, it involves a collapse of the volume and an increase in the oxygen coordination number around In and Nb cations. This behavior is very different from those of the rest of the studied wolframites.[5,14] Furthermore, $InNbO_4$ has a bulk modulus of 179(2) GPa,[13] which makes it the least compressible wolframite studied up to now.[5]

The differences between the HP behavior of $InNbO_4$ and the HP behaviors of other wolframites could be related to differences among the electronic configurations of cations or to the different formal charges of the cations.[1] If the second hypothesis is correct, similar behaviors should be followed by both $ScNbO_4$ and $InNbO_4$.[1] However, if the presence of indium leads to the distinctive HP behavior of $InNbO_4$, $ScNbO_4$ should have a different HP response than $InNbO_4$.[1] This is because of the different electronic and (semi)core electron configurations of In^{3+} ($[Kr]4d^{10}5s^05p^0$) and Sc^{3+} ($[Ar]3d^04s^0$), which will make the InO_6 and ScO_6 octahedra have different polyhedral compressibilities, as seen when comparing the HP behaviors of $InVO_4$ and $ScVO_4$.[15]

On the basis of the above-described facts, we believe it is timely to investigate the HP properties of $ScNbO_4$ to gain a better understanding of the behaviors of wolframite-type oxides under compression. In order to do this, we will perform a density functional theory (DFT) study of the structural, vibrational, elastic, and electronic properties of $ScNbO_4$ at ambient pressure and under compression. Furthermore, by considering different potential polymorphs, we will explore the existence of pressure-driven phase transitions. DFT has proven to be a useful framework for understanding materials properties quite broadly and, in many cases, even predicting behaviors that are later confirmed by experiments.[16] Also, we will explore the role of bonding in the high-pressure properties of $ScNbO_4$ within the framework of the quantum theory of atoms in a molecule (QTAIM).[17] In addition to calculations, in order to test the results of computer simulations, we have synthesized $ScNbO_4$ and characterized it by powder X-ray diffraction (XRD) at ambient conditions (298 K and 10^{-4} GPa) and by Raman spectroscopy and optical absorption both at ambient conditions and under HP.

METHODS

Experimental Details. Polycrystalline $ScNbO_4$ was synthesized by a solid-state synthesis from a mixture of high-purity (>99.9%) predried Sc_2O_3 and Nb_2O_5. The synthesis method was designed after the method commonly used to synthesize rare-earth niobates.[18] The starting oxides were weighed in a stoichiometric (1:1) ratio, exhaustively ground with a pestle and mortar, compacted by cold pressing into cylinders (12.5 mm in diameter and 5 mm in height), and finally heated at 1200 °C for 24 h in a single heat treatment. The formation of a single phase of $ScNbO_4$ was confirmed by powder XRD measurements performed using a Panalytical X-pert Pro diffractometer with Cu Kα radiation (λ = 1.5406 Å). The zero error in the powder XRD data was accounted for by using a LaB_6 crystallographic standard. No zero error was found in the setup. Raman measurements were carried out in the backscattering geometry using a single monochromator coupled with an edge filter and a thermoelectric-cooled charged coupled device (CCD) detector. The entrance slit was kept at 50 μm, which gives a spectral bandpass of 3 cm^{-1}, and the spectra could be reproduced with an accuracy of ±0.2 cm^{-1}. A green laser with 532 nm wavelength was used to excite the Raman modes. Observed peaks were fitted with Lorentzian line shape functions to get peak positions. The optical absorption of $ScNbO_4$ was measured in thin platelets obtained from compressed powder in the ultraviolet region using the setup described by Segura et al.[19] High-pressure experiments were carried out in diamond anvil cells using stainless steel gaskets. The pressure medium used in the experiments was a 16:3:1 methanol ethanol−water mixture, and pressure was determined using the ruby scale.[20]

Calculation Details. First-principles DFT calculations, at zero temperature, were performed by using the Vienna Ab initio Simulation Package (VASP).[21,22] The ion−electron interactions were described by using the projector augmented plane wave potential (PAW).[23] To describe the exchange−correlation energy, we have employed the Perdew−Burke−Ernzerhof for solids (PBEsol) functional within the general-gradient approximation (GGA)[24] and also the Heyd−Scuseria−Ernzerhof (HSE) hybrid density functional (HSE06).[25] The convergence criterion of the self-consistency process between successive iterations was set at 10^{-8} eV, and the Hellmann−Feynman force on each relaxed atom was less than 0.006 eV/Å. Due to the presence of oxygen in the investigated material, the set of plane waves was extended up to a kinetic energy cutoff of 700 eV. The integrations over the Brillouin zone (BZ) of wolframite and the other polymorphs of $ScNbO_4$ were calculated with a dense Monkhorst−Pack grid of special k points. The lattice-dynamic calculations were performed by means of the open tool Phonopy.[26] Vibrational modes were then estimated within the framework of density functional perturbation theory (DFPT).[27] Due to the ionic trend of the investigated compounds and in order to remove the degeneracy between the longitudinal optical (LO) and transverse optical (TO) phonons at the Brillouin zone center, the LO−TO splitting was taken into account on a 3 × 3 × 3 supercell. Finally, to study the mechanical stability of the ambient structure, the elastic stiffness constants were calculated within the stress method.[28]

To analyze the covalent and ionic counterparts in our materials, we used the noncovalent interactions index (NCI),[29,30] which is calculated using the reduced density gradient of the electron density (ρ), where the density varies gradually. This characterization was carried out within the framework of the quantum theory of atoms in molecules (QTAIM),[17] as defined by

$$\mathrm{NCI} = s = \frac{1}{2(3\pi^2)^{1/3}} \frac{|\nabla\rho|}{\rho^{4/3}} \quad (1)$$

The 4/3 density exponent guarantees that s is a dimensionless quantity. The properties of $s(\mathbf{r})$ isosurfaces are determined by their critical points.[29,30] The significance of the NCI isosurface is based on the sign of the second eigenvalue of the Hessian (λ_2) multiplied by the electron density. If the result is negative, the attractions are judged attractive and the isosurface is colored in blue. However, if it is positive, the attractions are judged repulsive and the corresponding

https://doi.org/10.1021/acs.jpcc.1c10483
J. Phys. Chem. C 2022, 126, 4664−4676

Table 1. Unit Cell Parameters and Volume at Ambient Pressure Calculated for Wolframite-Type $ScNbO_4$[a]

	a (Å)	b (Å)	c (Å)	V_0 (Å^3)	B_0 (GPa)	B_0'	β (deg)
this work (calc, PBEsol)	4.8233	5.7035	5.1029	140.36	178	4.9	91.00
this work (calc, HSE06)	4.8380	5.7023	5.1032	140.77	176	4.8	90.87
this work (expt)	4.7997(3)	5.6494(3)	5.0842(3)	137.86(9)	–	–	91.42(4)
expt[9]	4.8091	5.6652	5.1011	138.98	–	–	90.25
expt[31]	4.8067	5.6689	5.1045	139.04	–	–	91.46

[a]Our calculations (calc) are compared with the present and previous experiments[9,31] (expt). The calculated bulk modulus and its first derivative are also included.

Table 2. Comparison of the Experimental[9] and DFT Calculated Atomic Coordinates of Monoclinic Wolframite-Type $ScNbO_4$ (Space Group $P2/c$) at Ambient Pressure[a]

		experiment			calculation PBEsol			calculation HSE06		
atom	site	x	y	z	x	y	z	x	y	z
Sc	2f	0.5	0.6825(5)	0.25	0.5	0.68071	0.25	0.5	0.68509	0.25
Nb	2e	0	0.1725(5)	0.25	0	0.18313	0.25	0	0.18189	0.25
O_1	4g	0.222(1)	0.898(1)	0.439(1)	0.22205	0.89286	0.43489	0.21785	0.89509	0.43720
O_2	4g	0.260(1)	0.386(1)	0.409(1)	0.26010	0.38316	0.40775	0.26327	0.38757	0.40836

[a]The column "site" gives the Wyckoff position of each atom.

domains are colored in red. In the case where $(\lambda_2)\rho$ is close to zero, weak interactions such as van der Waals interactions or hydrogen bonds are invoked, and the isosurfaces are depicted in green.

RESULTS AND DISCUSSION

Structural Properties and Equation of State. Let us start our discussion by characterizing $ScNbO_4$ under ambient conditions. We will start with the structural characterization. We show in Figure 1 a powder XRD pattern of the synthesized material. Figure 1 includes a Rietveld refinement which confirms that our sample crystallizes in the wolframite-type structure. In the XRD pattern, we have not detected impurities or minority phases within the accuracy of the experiment. The crystal structure of $ScNbO_4$ has been previously reported by Keller using space group $P2/a$.[9] However, we will use space group $P2/c$ (unique axis b) to describe it, because it is the usual description of wolframites[5] and the standard setting according to the International Union of Crystallography. The measured unit cell parameters are a = 4.7997(3) Å, b = 5.6494(3) Å, c = 5.0842(3) Å, and β = 91.42(4)°, in very close agreement with the literature.[9,31] The goodness-of-fit factors of the refinement are R_P = 9.5%, R_{WP} = 12.4%, and χ^2 = 2.6. These values support a correct structural assignment.

We will now use the results of experiments to validate the results of computer simulations. We have optimized the structure of $ScNbO_4$ at zero pressure by means of DFT calculations. The two approaches we used gave very similar results regarding the crystal structure as can be seen in Table 1, where the obtained lattice parameters are summarized and compared with results from experiments.[9,31] The calculated atomic positions are provided in Table 2 and compared with those from a previous experiment.[9] We can see that the deviations between calculated and measured lattice parameters are less than 0.5, 1, 0.4, and 0.1% for a, b, c, and β, respectively. The small overestimation of the unit cell volume by calculations is within the typical errors of GGA calculations.[32] The agreement for the atomic positions is also excellent. This implies that the GGA-PBEsol and HSE06 functionals accurately describe the crystal structure of $ScNbO_4$ at ambient conditions. Furthermore, we used a third-order Birch–Murnaghan equation of state (EOS)[33] to calculate the bulk modulus and its derivative. These parameters were derived from the energy (E) versus volume (V) curve shown in Figure 2. The volume at zero pressure (V_0), bulk modulus (B_0), and first pressure derivative (B_0') are presented in Table 1. Both calculations methods give similar results.

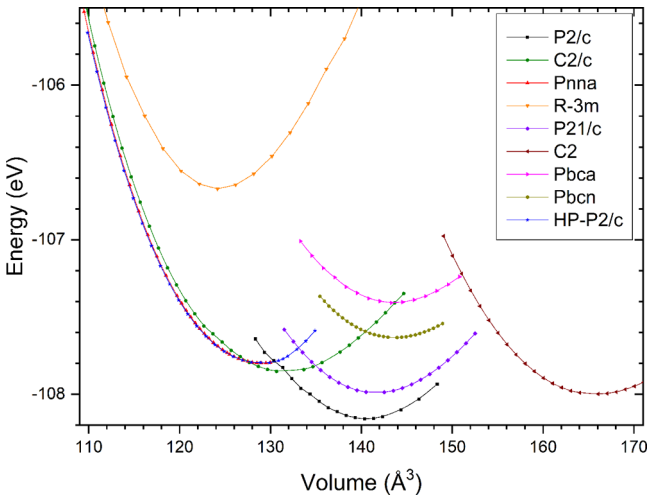

Figure 2. Energy versus volume plot for the different model structures in this work. Symbols stand for the calculated values, whereas lines are a guide to the eye. To facilitate comparison, volumes have been normalized assuming two formula units per unit cell (Z = 2) as in wolframite. The structures are named by their space group (see text). HP-$P2/c$ is used to distinguish the HP structure described by space group $P2/c$ from low-pressure wolframite, named as $P2/c$.

The bulk modulus value we have determined for $ScNbO_4$ (176–178 GPa) is comparable to the value predicted assuming the NbO_6 octahedron is a rigid and noncompressible unit[5] (187 GPa) and is nearly identical to the bulk modulus of $InNbO_4$ (179 GPa).[13] These two compounds are less compressible than any other wolframite. Apparently this feature is independent of the specific electronic configuration of In and Sc. In other MTO_4 wolframites, it has been found that the bulk modulus is mainly determined by the

https://doi.org/10.1021/acs.jpcc.1c10483
J. Phys. Chem. C 2022, 126, 4664–4676

Table 3. Calculated Elastic Constants (C_{ij} in GPa) of Wolframite-Type $ScNbO_4$ and Values of Bulk Modulus (K), Young's Modulus (E), and Shear Modulus (G)[a]

C_{11}	C_{12}	C_{13}	C_{15}	C_{22}	C_{23}	C_{25}	C_{33}	C_{35}	C_{44}	C_{46}	C_{55}	C_{66}
286.404	94.156	153.070	16.688	238.070	229.778	145.653	−17.651	277.716	59.881	−22.069	90.943	59.689
K_V		K_R		K_H		E_V		E_R		E_H		
175.517		169.551		172.534		182.635		161.136		171.885		
G_V		G_R		G_H								
68.837		60.053		64.445								

[a]K, E, and G were calculated using the Voigt (V), Reuss (R), and Hill (H) approximations. Units are GPa.

compressibility of the MO_6 octahedra.[5] As a first approximation, bond compressibility within the MO_6 octahedron is inversely proportional to the formal cation charge.[34] Thus, the fact that In and Sc are trivalent, while in other wolframites the equivalent cation is divalent, is what makes the ScO_6 and InO_6 polyhedra much less compressible than MO_6 octahedra in isomorphic compounds; making $ScNbO_4$ and $InNbO_4$ the wolframites with the largest known bulk moduli.

Elastic Constant Calculations. We have also evaluated the mechanical properties of $ScNbO_4$. This task has been accomplished by calculating the response of $ScNbO_4$ to a variety of strains.[35,36] In this way, we obtain the elastic constant, which helps in the analysis of the mechanical stability and mechanical properties of the compound. The stiffness matrix eigenvalues λ_i (i = 1, ..., 6) have also been calculated, as shown in Table S1. They are all positive at ambient pressure, thus satisfying the Born elastic stability criteria.[37] Then, $ScNbO_4$ is mechanically stable in the monoclinic $P2/c$ structure. The calculated elastic constants are collected in Table 3. Further, elastic moduli derived from the elastic constants have been calculated and are also reported in Table 3. We observe that the bulk modulus extracted from elastic components and denoted as K (169.5−175.5 GPa) agrees very well with theoretical values derived from EOS calculations (B_0 = 176−178 GPa), demonstrating the consistency of the current study. Thus, elastic constant calculations confirm that $ScNbO_4$ is a noncompressible material. On the other hand, the value of the Young's modulus (E) (161−182 GPa) indicates a large tensile (or compressive) stiffness of $ScNbO_4$ when a force is applied lengthwise. Regarding the shear modulus (G), its value (60−69 GPa) indicates shear deformations are favored over volume contraction in $ScNbO_4$, making it susceptible to nonhydrostatic stress.[38] Another piece of information we have obtained for ScNbO4 is the linear compressibility.[39] We have calculated it by the mean of the ELATE tool.[40] The results are shown in Figure S1. They demonstrate that the behavior of $ScNbO_4$ is anisotropic, making this compound more sensitive to pressure application in shear directions. According to the results, the unique b-axis is the most compressible axis.

Raman Experiments and Phonon Spectrum. Once the features of the mechanical properties of $ScNbO_4$ are known, it is time to analyze its vibrational properties at ambient pressure. We first present the Raman spectrum, which is given in Figure 3. Group theory analysis predicts a total of 18 Raman-active modes for the wolframite structure. Their representation at the center of the Brillouin zone is $\Gamma = 8A_g + 10B_g$.[35,41] All the expected modes have been detected in our experiment (Figure 3 and Table 4). Twelve modes are very strong, five of them are shoulders, like those around the strong mode (left and right sides) we have detected at 628 cm^{-1}, and the 18th mode comes from the mode near 280 cm^{-1} which is a doublet. Previous to our study, only the two strongest modes (at 628 and 827 cm^{-1} in our experiment) were detected in synthetic $ScNbO_4$.[42] On the other hand, Raman measurements have been performed on the natural mineral nioboheftetjernite, $(Sc_{0.40}Fe_{0.37}^{3+}Ti_{0.15}Mn_{0.08}^{2+})(Nb_{0.58}Ta_{0.33}W_{0.03}Ti_{0.03}Sn_{0.02})O_4$.[12] In this case, the reported Raman modes are consistent with the

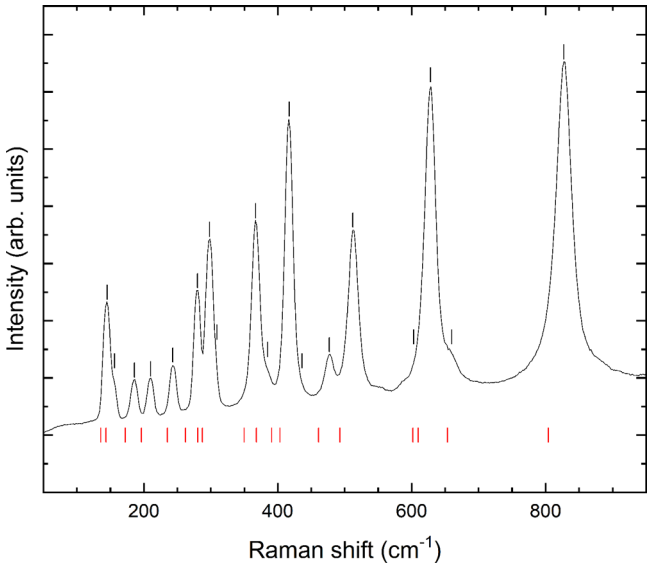

Figure 3. Raman spectrum of $ScNbO_4$. Black tick marks indicate the frequencies of the Raman modes identified in experiments. The red ticks indicate the calculated frequencies.

Table 4. Experimental and Calculated Frequencies (ω) of Raman modes[a]

		DFT calculations		
mode	expt ω (cm^{-1})	ω (cm^{-1})	R_ω	$InNbO_4$ ω (cm^{-1})
B_g	145	135.6	0.06	120
A_g	156	143.3	0.08	122
B_g	186	172.0	0.08	151
B_g	210	196.1	0.07	185
B_g	243	235.0	0.03	196
A_g	280	262.1	0.06	243
A_g	298	280.4	0.06	279
B_g	308	287.3	0.07	295
B_g	367	349.7	0.05	331
A_g	385	368.1	0.04	352
A_g	417	391.0	0.06	402
B_g	436	403.3	0.08	410
B_g	477	461.1	0.03	470
A_g	512	492.8	0.04	501
B_g	603	601.8	0.00	633
A_g	628	609.8	0.03	651
B_g	660	653.4	0.01	675
A_g	827	804.0	0.03	817

[a]The mode assignment is included as well as the relative difference between measured and calculated frequencies (R_ω). The Raman modes of isostructural $InNbO_4$ are included for comparison.

https://doi.org/10.1021/acs.jpcc.1c10483
J. Phys. Chem. C 2022, 126, 4664−4676

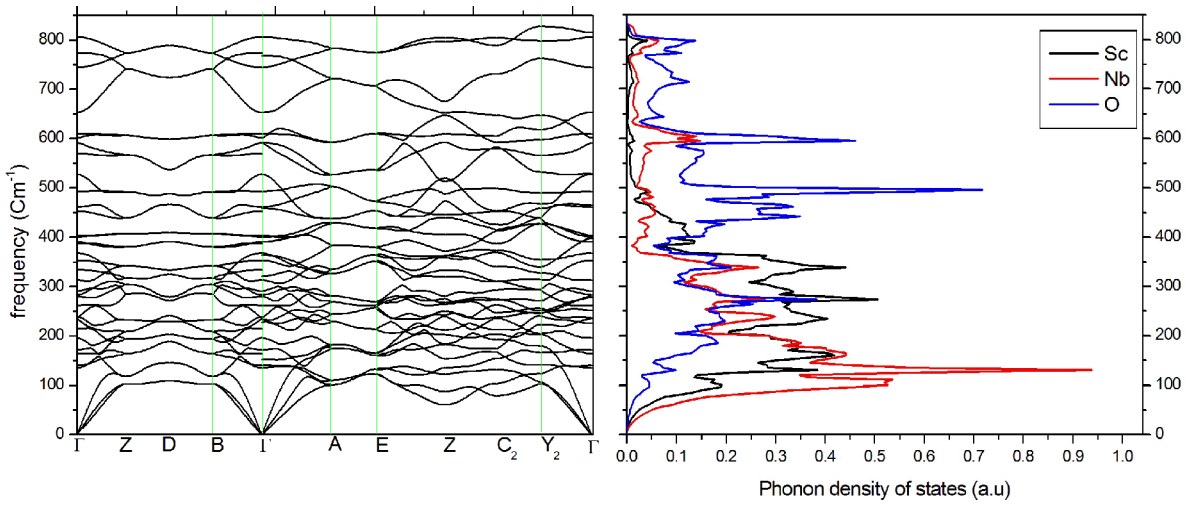

Figure 4. (left) Phonon dispersion curve and (right) phonon partial density of states of $ScNbO_4$ at ambient pressure.

modes we have detected at 145, 298, 385, 417, 628, and 827 cm^{-1}. In the two previous experiments, a weak mode was observed at 850 cm^{-1}, which was not observed in our experiments, and we believe it was caused by an overtone.

To display a full description of the vibrational modes, we have calculated the phonon dispersion spectrum of the $ScNbO_4$ at ambient pressure. They are presented in Figure 4. The absence of imaginary frequencies in the whole Brillouin zone confirms the dynamical stability of wolframite-type $ScNbO_4$. We can see that the phonon dispersion displays 36 branches corresponding to 3 acoustic and 33 optical modes. The analysis of the zone center phonon gives the following mechanical decomposition: $\Gamma = 8A_g + 8A_u + 10B_g + 10B_u$. $\Gamma_{acoustic} = A_u + 2B_u$, whereas $\Gamma_{optic} = 8A_g(R) + 7A_u(IR) + 10B_g(R) + 8B_u(IR)$. IR and R denote the infrared- and Raman-active modes, respectively. In Table 4 we include the calculated frequencies of Raman modes and the mode assignment which was obtained from calculations. As can be seen in Table 4, there is a small systematic underestimation of DFT calculated phonon frequencies. The relative difference is smaller than 3% for the modes with frequencies above 603 cm^{-1} and below 3.8% for the two modes at 477 and 491 cm^{-1}. For the rest of the modes, the differences between experiments and calculations are between 3 and 8%. The largest discrepancy is observed for the A_g mode with frequency 156 cm^{-1}; see Table 4. Notice that these differences are of the same order as those observed in other ternary oxides in which the literature considers that the agreement between experiments and calculations is good.[43,44] A possible reason for the mode-frequency underestimation could be related to the small volume overestimation in DFT calculations, which usually leads to an underestimation of restoring forces associated with phonons and consequently of phonon frequencies.[45] A deep discussion of the reasons for the better agreement for modes measured above 477 cm^{-1} is beyond the scope of this work. We will just mention here that the six high-frequency modes in wolframites are usually associated with internal stretching vibrations of the NbO_6 octahedra, while modes measured below 477 cm^{-1} involve motions of the NbO_6 octahedra as rigid units against the Sc atom.[46] The frequencies of the internal stretching modes are higher than those of the external modes because the internal bonding within the NbO_6 octahedra is stronger than the external lattice binding. This fact is consistent with the assumption that the NbO_6 octahedron behaves as a rigid unit.[5] It is a common argument in the literature that the internal (molecular) modes are better described than the external (collective) modes.[47] It is not surprising that we have observed the same fact in $ScNbO_4$. We would only add here that the Raman spectrum of $ScNbO_4$ is qualitatively similar to that of isostructural $InNbO_4$.[13] In particular, frequencies in the high-frequency region, originated by internal vibrations of the NbO_4 tetrahedron,[13] are very similar in both compounds. This can be seen in Table 4, where the frequencies of both compounds are compared. Notice that the frequency of the lowest frequency mode is slightly higher in $ScNbO_4$ than in $InNbO_4$, due to the smaller mass of Sc.

Electronic Properties. There is conflicting information in the literature about the energy and nature of the band gap of $ScNbO_4$. From the luminescence experiments reported by Brixner,[31] it can be concluded that $ScNbO_4$ is a direct band gap material with a band gap energy (E_{gap}) of ~4.77 eV. In contrast, DFT calculations performed using the GGA approximation and the PBE exchange functionals[11] reported that $ScNbO_4$ is an indirect band gap material with E_{gap} = 3.93 eV. However, our own DFT calculations using the HSE06 approximation lead to the same conclusion as Brixner's experiments regarding the direct nature of the band gap. In order to clarify this discrepancy, we have measured the optical absorption spectrum of $ScNbO_4$. The spectrum is shown in Figure 5. It has a sharp absorption edge around 4.8 eV, suggesting a direct band gap plus a weak absorption tail at lower energies, which corresponds to a subgap absorption related to the presence of defects, which has also been observed in diffuse reflectance experiments.[42] Assuming a direct band gap from the square of the absorption coefficient (α), we found E_{gap} = 4.82(2) eV, which agrees well with conclusions from luminescence measurements.[31] Furthermore, we have also performed band structure calculations using the HSE06 hybrid density functional.[25] This has been done to overcome the fact that the conventional PBE and PBEsol functionals underestimate E_{gap}. Figure 6a shows the calculated band structure of $ScNO_4$ under this approach. The calculated band gap energy is 4.88 eV, very close to the experimental value. These calculations also support that the band gap is direct with the maximum (minimum) of the valence (conduction) band located at the high-symmetry Γ point.

https://doi.org/10.1021/acs.jpcc.1c10483
J. Phys. Chem. C 2022, 126, 4664−4676

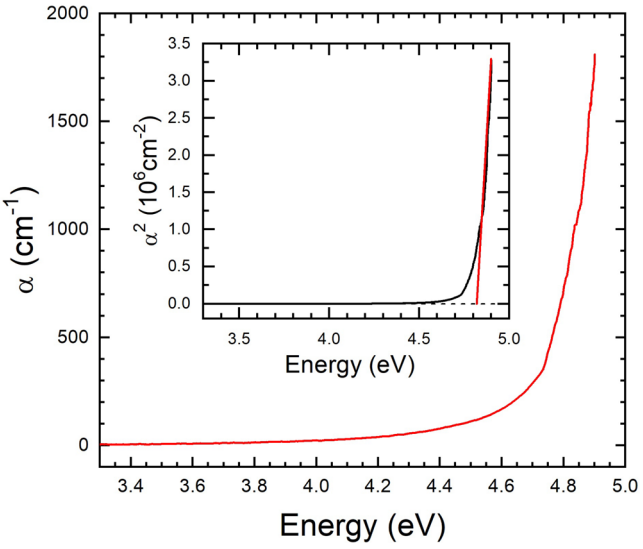

Figure 5. Absorption coefficient (α) of $ScNbO_4$ as a function of photon energy at ambient pressure. The inset shows the plot of α^2 used to determine the band gap energy.

To deeply analyze the contribution of each orbital to the electronic properties, we have also calculated the electron density of states and their projections. These results are provided in Figure 6b,c. The plots show that the orbitals in the top of the valence band are mainly occupied by O 2p states. On the other hand, the orbitals in the bottom of the conduction band are mainly contributed by O 2p and Nb 4d orbitals, with a small contribution of Sc 3d orbitals. This arrangement or orbital contributions suggests that the band gap value is primarily determined by the molecular electronic structure of the NbO_4^{3-} unit.[48,49] Furthermore, we also note a strong Nb d/O p and Sc d/O p hybridization that occurs near the Fermi level. This and the low electronegativity of the Sc/Nb atoms compared to that of the oxygen one suggests a possible mix of covalent−ionic bonding nature.

Bonding Properties. To complete the characterization of $ScNbO_4$ at ambient pressure, we will analyze its bonding. This analysis can be done by studying the electron density $\rho(r)$ and its derived scalar and vector fields. We have calculated the electron density of $ScNbO_4$ and displayed it in Figure 7a. The QTAIM strategy is used to decompose $\rho(r)$ in the real-space framework. This method encompasses several methods for estimating the ionicity degree of the title compound.[50,51] We obtained a degree of ionicity of 61% by simply adding the ratios of the effective charges ($Q(\Omega)$) of Sc, Nb, and O atoms to their corresponding nominal oxidation states ($OS(\Omega)$). This result indicates that the bonding pattern of the $ScNbO_4$ at ambient pressure is far from pure ionic.

The reduced density gradient ($s(\mathbf{r})$) was also used to deeply analyze the bonding properties of the investigated material. This index takes as a key point the very low values of $\rho(r) \to 0$; see Figure 7a. The situation that such points encompass can be understood as the lower bound or an absence of charges, which represents a critical bond point (BCP) in the language of the QTAIM approach.[29] The reduced density gradient has no upper bound and is maximal when the density disappears faster than the gradient, resulting in $s(r) \to \infty$. $s(\mathbf{r})$ was calculated in its 2D map and 3D isosurfaces, and the results are shown in Figure 7b,c. Here, the NCI index integrates the $\text{sign}(\lambda_2)\rho$ to reveal the attractive, repulsive, or weak nature of the interaction. $\text{sign}(\lambda_2)\rho$ is the sign of the second eigenvalue of the Hessian matrix of ρ. The top of Figure 7c gives a global representation of all the interactions found in the bonding pattern of $ScNbO_4$. However, we have also dissected this plot into attractive and repulsive contributions. The result shows a disk-like shape in blue, indicating a highly localized interaction in the middle of Sc−O bonds, the signature of strong attractive interactions. Furthermore, some domains show a balance between repulsive and attractive interactions between Nb and O atoms. In Figure 7c1,c2, we isolated the interactions of negative and positive $\text{sign}(\lambda_2)\rho$ results; the panel labeled "2" shows a red circle, indicating some repulsive interactions along the Sc−O bonds. This means that Sc−O bonds are governed by a mix of ionic and covalent natures. Otherwise, to deeply analyze the nature of the bonding pattern, we made a partition of electronic basins based on the electron localization function (ELF)[52] (see details in the Supporting Information). We found that only the Sc and O atoms share electrons, giving rise to a valence disynaptic V(Sc,O) basin. However, $\eta(\vec{r})$ for V(Sc,O) gives a value of 0.86, a signature of nonperfect covalent bonds (usually accounted for ELF = 0.9).[52,53] The Nb atom, on the other hand, has only a monosynaptic basin (V(Nb)). The value of the ELF attractor related to V(Nb) gives a value of about ∼0.8, which is the signature of rather more ionic bonds; see both Table S2 and Figure S3. It can also be seen that the

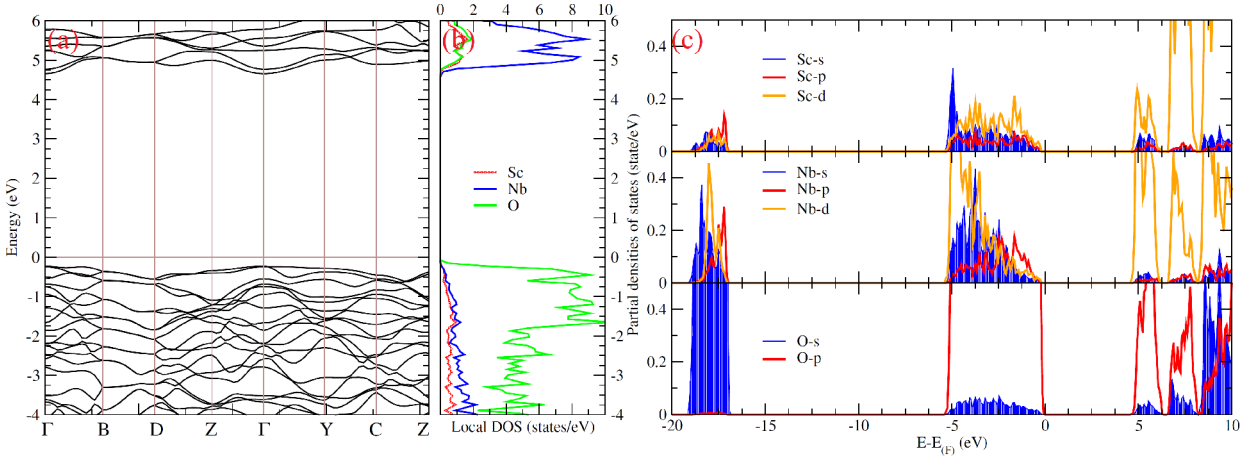

Figure 6. (a) Band structure, (b) local DOS, and (c) partial density of states of $ScNbO_4$ at ambient pressure.

https://doi.org/10.1021/acs.jpcc.1c10483
J. Phys. Chem. C 2022, 126, 4664−4676

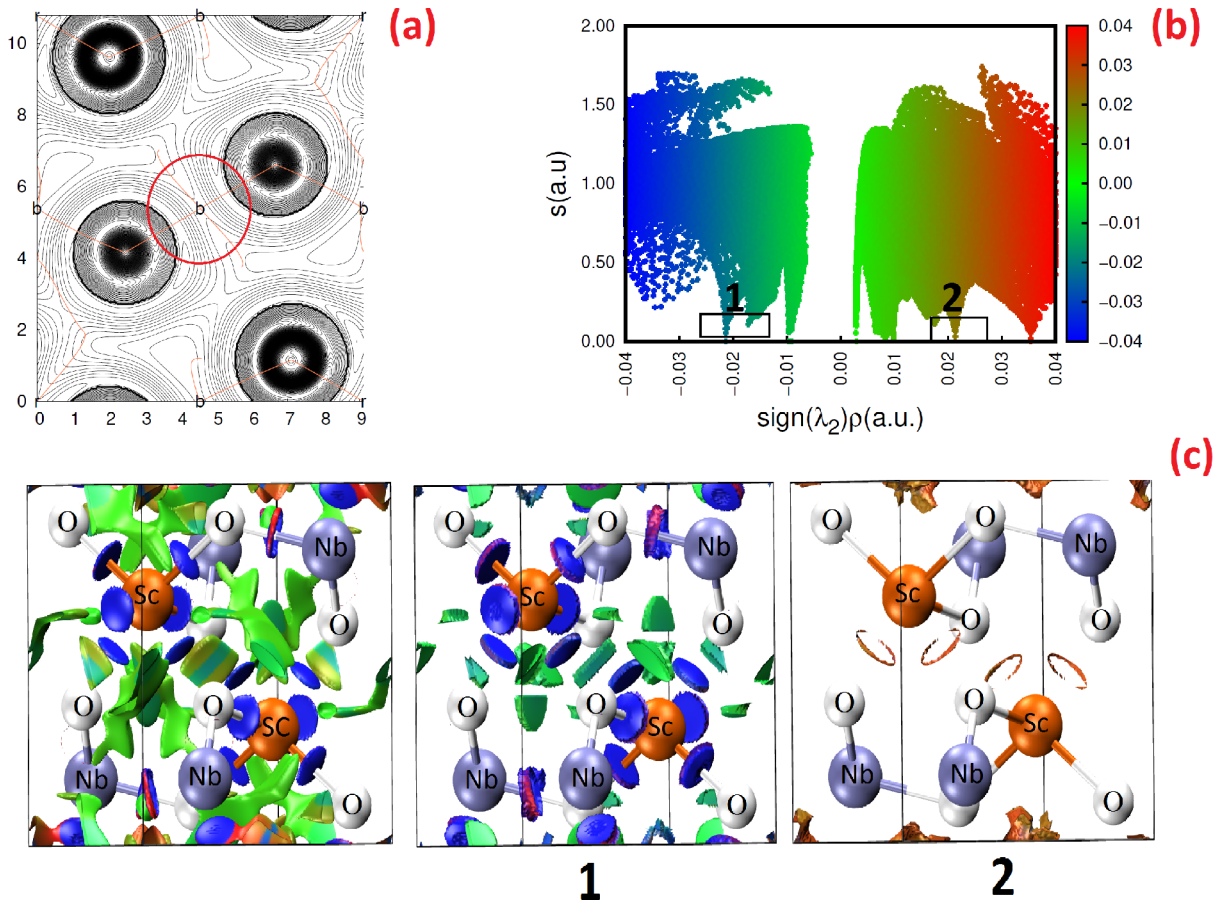

Figure 7. (a) Topological analysis of electron density, and NCI analysis. (b) Two-dimensional map. (c) Three-dimensional isosurfaces. Surfaces are colored in the range of [−0.04, 0.04] au of sign($(\lambda_2)\rho(\mathbf{r})$) (isovalue s = 0.4 au). Repulsive interactions are shown as red isosurfaces, van der Waals interactions are shown as delocalized green regions, and strong attractive interactions are shown as localized blue lentils. Parts 1 and 2 give the NCI analysis taken at regions 1 (sign($(\lambda_2)\rho(\mathbf{r})$) < 0) and 2 (sign($(\lambda_2)\rho(\mathbf{r})$) > 0) of the zero BCPs, respectively.

localization domain V(Sc,O) has a different basin population than the nonperfect covalent Sc−O bond's two-electron signature. The ELF topology shows that the basin sphericity of oxygen atoms is deformed with different populations, a sign of polarized basins, which confirms the main ionic character of Nb−O bonds. Nevertheless, the ELF population analysis, provided in Table S2, shows a more subtle scheme.

$ScNbO_4$ under High Pressure. Let us now look at the structural stability of $ScNbO_4$ under hydrostatic compression and the influence of pressure on the physical properties of $ScNbO_4$. By means of total-energy DFT calculations, we have tested the structural stability of $ScNbO_4$ assuming several candidate structures. Since PBEsol and HSE06 give very similar descriptions of wolframite-type $ScNbO_4$ but HSE06 involves more use of memory and CPU time than PBEsol, calculations as a function of pressure to explore possible phase transitions, considering different structures, have been carried out only with PBEsol. The structures considered in the calculations have been chosen on the basis of crystal-chemical arguments commonly used for wolframite-type MTO_4 oxides and Bastide's diagram.[1] We have specifically considered for computer simulations the stable wolframite-type polymorph of $ScNbO_4$ (space group $P2/c$) and as, potential HP polymorphs, crystal structures isomorphic to α-$BiNbO_4$ (space group $Pnna$), β-$BiNbO_4$ (space group $C2$), $SrTeO_4$ (space group $Pbca$), $SnWO_4$ (space group $Pbcn$), $CaUO_4$ (space group $R\bar{3}m$), $LaNbO_4$ (space group $C2/c$), the HP phase of $HoNbO_4$ (space group $P2_1/c$), and the HP phase of $InNbO_4$ (space group $P2/c$). In this article, we name this structure as HP-$P2/c$ to distinguish it from wolframite.

The enthalpy calculations plotted in Figure 8 support that the wolframite-type polymorph is the most stable at ambient pressure. Figure 8 also supports the occurrence of a phase transition at ∼5 GPa to an orthorhombic structure isomorphic to α-$BiNbO_4$ (space group $Pnna$) and a subsequent transition at ∼11 GPa to a polymorph isomorphic to the HP phase of $InNbO_4$ (space group $P2/c$, named as HP-$P2/c$ in Figure 8).[13] The structural information on the two HP phases predicted by calculations is summarized in Table 5. The existence of phase transitions at similar pressures has been confirmed by HP Raman and optical absorption experiments, which will be presented and discussed toward the end of this work. For the rest of the article, we will refer to the proposed HP phases as HP1 (space group $Pnna$) and HP2 (phase described by space group $P2/c$ stable beyond ∼11 GPa).

Interestingly, the orthorhombic HP1 structure belongs to space group $Pnna$, which is a supergroup of space group $P2/a$ (which is equivalent to $P2/c$). By using group−subgroup relationships, we can find that HP1 can be seen as a symmetry-enhanced supercell of wolframite, with with the a- and c-axes very similar, the β angle equal to 90°, and the unit cell doubled by multiplying by 2 the b-axis of wolframite, which abruptly decreases at the transition. In fact, the HP1 structure can be described as pseudotetragonal. Regarding polyhedral units, the

https://doi.org/10.1021/acs.jpcc.1c10483
J. Phys. Chem. C 2022, 126, 4664−4676

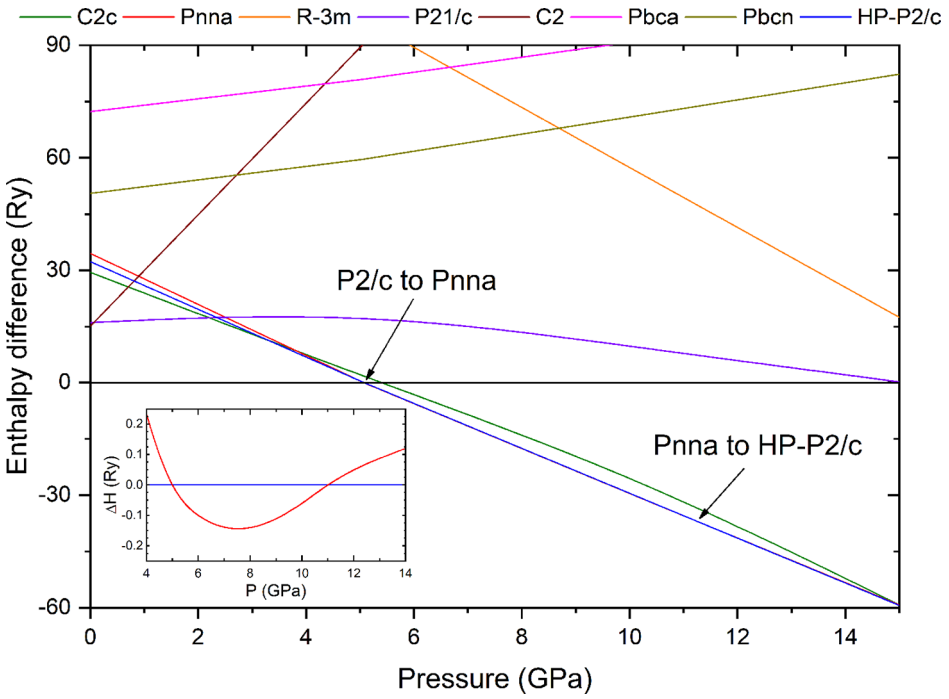

Figure 8. Pressure dependence of the enthalpy difference between candidate structures and the wolframite ($P2/c$) phase. Different phases are labeled by the space group of the structure (see text). In the inset we represent the enthalpy difference between the HP1 (*Pnna*) and HP2 structures (HP-$P2/c$) which cannot be distinguished in the main figure.

Table 5. Structural Parameters of HP1 $ScNbO_4$ (Space Group *Pnna*) at 5.36 GPa and HP2 $ScNbO_4$ (Space Group $P2/c$) at 11.1 GPa

a = 5.079 Å	b = 9.834 Å	c = 5.075 Å	β = 90.00°
HP1 at 5.36 GPa			
atom	x	y	z
Sc(2f)	0.75000	0.00000	0.25000
Nb(2e)	0.25004	0.25000	0.25000
O_1(4g)	0.54492	0.37542	0.95515
O_2(4g)	0.04492	0.12458	0.45515
a = 4.887 Å	b = 4.998 Å	c = 4.995 Å	β = 90.094°
HP2 at 11.1 GPa			
atom	x	y	z
Sc(2f)	0.50000	0.25018	0.25000
Nb(2e)	0.00000	0.75058	0.25000
O_1(4g)	0.25069	−0.04260	0.04136
O_2(4g)	0.25080	0.54257	0.45756

phase transition to HP1 involves a change in the coordination numbers of Sc and Nb. In phase HP1, Sc and Nb atoms are coordinated to eight oxygen atoms, forming dodecahedral units. The same kind of coordination is found in phase HP2.

Figure 9 shows the pressure dependence of the unit cell parameters and volume of the wolframite phase (also named as LP) and phases HP1 and HP2. At both phase transitions, there is a discontinuity in the unit cell volume, which indicates that they are first-order transitions. Under compression, the behavior of the LP phase is slightly anisotropic. Since the LP phase is monoclinic, to analyze the compressibility of the structure it is necessary to obtain the main axis of compression of the compressibility tensor.[54] We have found that the three eigenvalues of the compressibility tensor are κ_1 = 2.42(6) × 10^{-3} GPa^{-1}, κ_2 = 1.75(6) × 10^{-3} GPa^{-1}, and κ_3 = 1.44(6) × 10^{-3} GPa^{-1}. They correspond to the [0 1 0], [−5 0 4], and [10 0 11] directions, which are the axes of maximum, intermediate, and minimum compressibility directions, respectively. Noticeably, the most compressible axis is the unique b-axis. This trend has already been seen in wolframite-type $InNbO_4$, which presents a close structural response to compression.[13] Notice that the same nonisotropic behavior is supported by elastic constant calculations as reported above (see also Figure S1).

For phase HP1, which is orthorhombic, the axial compressibilities are found to be κ_a = 2.11(6) × 10^{-3} GPa^{-1}, κ_b = 1.20(6) × 10^{-3} GPa^{-1} and κ_c = 1.66(6) × 10^{-3} GPa^{-1}. Furthermore, the three main compressibilities for the monoclinic phase HP2 are κ_1 = 1.66(4) × 10^{-3} GPa^{-1}, κ_2 = 1.60(3) × 10^{-3} GPa^{-1}, and κ_3 = 1.16(4) × 10^{-3} GPa^{-1}. The main compressibility directions are [0 1 0], [−1 0 4], and [4 0 1], respectively. The axial compressibilities decrease following the sequence LP → HP1 → HP2 because of the enhancement of the packing efficiency.

A third-order Birch−Murnaghan equation of state (BM-EOS)[33] was employed to fit the volume versus pressure curves for phases LP, HP1, and HP2; see Figure 9. The plot indicates that a phase transition causes an important collapse of unit cells of 9% between the monoclinic LP and orthorhombic HP phases. On the other hand, the collapse between phases HP1 and HP2 is 1%. The EOS parameters of phase HP1 are V_0 = 260.6 $Å^3$, B_0 = 187 GPa, and B_0' = 4.5. The EOS parameters of the phase HP2 are V_0 = 128.4 $Å^3$, B_0 = 196 GPa, and B_0' = 3.9. Interestingly, under compression, the crystal structure of the monoclinic phase HP2 becomes virtually tetragonal at 20 GPa. This suggests a possible third phase transition to one structure described by a tetragonal maximal supergroup of $P2/c$, for instance $P4/mmc$. The identification of the structure of a potential third HP phase is beyond the scope of this work.

Raman experiments under compression up to 18.2 GPa confirm the existence of two phase transitions. The spectra measured under increasing pressure are shown in Figure 10. In

https://doi.org/10.1021/acs.jpcc.1c10483
J. Phys. Chem. C 2022, 126, 4664−4676

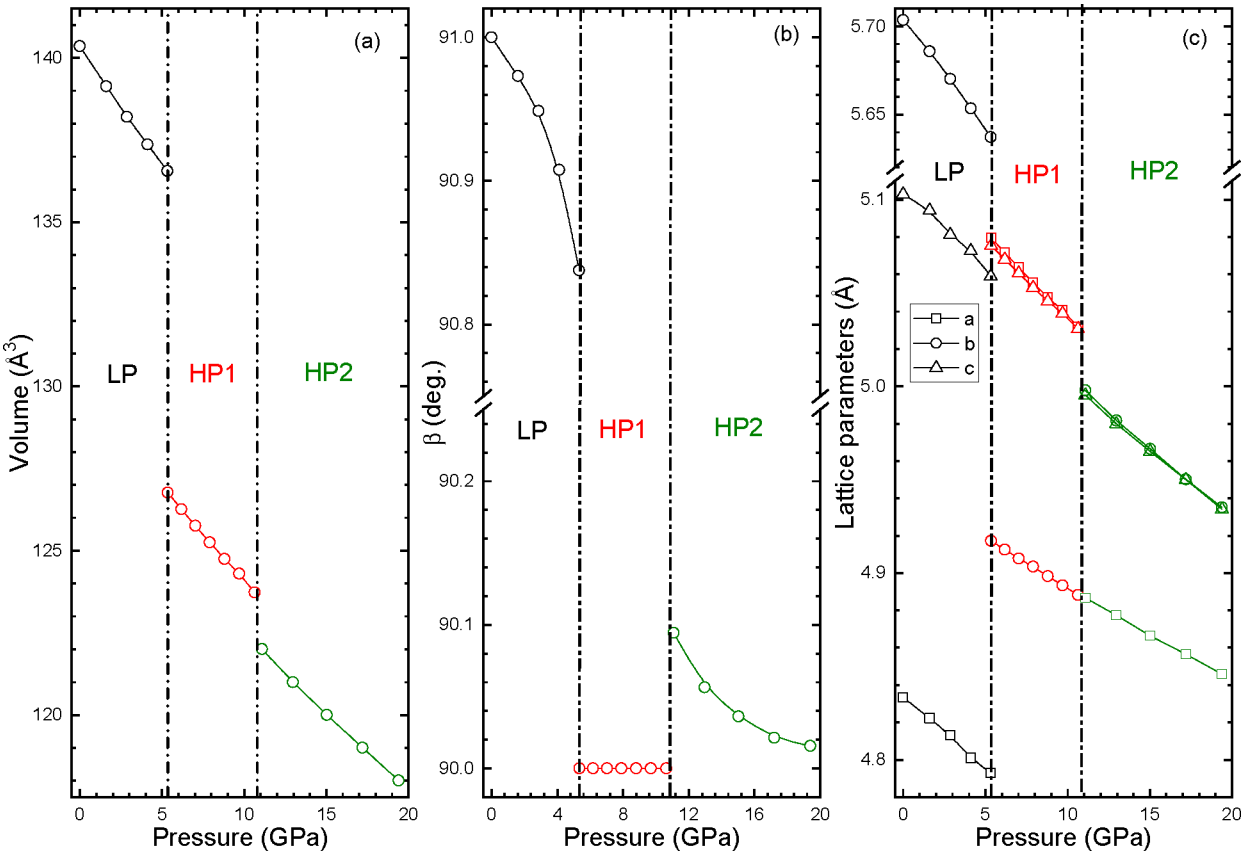

Figure 9. Pressure dependence of (a) volume of the unit cell (for phase HP1 we plotted $V/2$ to facilitate comparison), (b) β angle, and (c) lattice parameters of $ScNbO_4$. For the volume the lines are the results of the BM-EOS fits. For the other panels they are guide to the eyes. Vertical lines indicate transition pressures. Black, red, and green colors have been used for the LP, HP1, and HP2 phases, respectively. For the unit cell parameters (a, b, and c) we used different symbols which are indicated in the inset. For phase HP1 $b/2$ is plotted to facilitate comparison.

the experiments, we have detected the appearance of additional peaks at 3.7 GPa (depicted by asterisks in Figure 10). These peaks become stronger as pressure increases, while the peaks of the low-pressure phase become weaker and disappear at 4.2 GPa. This indicates the occurrence of a phase transition, which is in agreement with the theoretical prediction of a phase transition to an orthorhombic structure near ∼5 GPa. The number of Raman modes in the HP phase is 19, which is in agreement with the increase in the number of Raman modes at the phase transition according to group theory (see discussion below). Under further compression, additional qualitative changes take place in the Raman spectrum at 10.4 GPa, indicating a second phase transition, which is also in agreement with DFT calculations. The second transition is less evident than the first one, but in a close look at Figure 10 it can be seen that there are peaks becoming weaker above 6.9 GPa (for instance, the peak marked by the pound signs) and a new peak appearing at 10.4 GPa. In addition, we have found discontinuities in phonon frequencies and changes in their pressure dependence that evidence the occurrence of the phase transition and will be discussed next. The second HP phase remains stable up to 18.2 GPa, the highest pressure covered by our Raman experiments. However, the Raman spectra gradually deteriorate beyond 13.9 GPa due to the enhancement of nonhydrostatic effects.[55] It should be noticed that the hydrostatic limit of the used pressure medium (16:3:1 methanol ethanol−water) is 10.5 GPa.[55] This pressure is very similar to the pressure where the second phase transition takes place (10.4 GPa). Then there is a possibility that the phase transition could be influenced by shear. However, this issue is beyond the scope of this work and should be resolved in the future by means of fully hydrostatic studies. All changes observed are reversible, with the Raman spectrum of the low-pressure phase fully recovered after decompression (see Figure S4). Interestingly, both of the experimentally observed phase transition points are at a lower pressure than the calculations indicate. This thing could be related to the fact that calculations have been carried out at 0 K temperature.

From the results shown in Figure 10 we have obtained the pressure dependence of all observed Raman modes. The results are shown in Figure 11. In the LP phase, we could follow 17 out of the 18 modes under compression. The missing mode is a weak one that is not detected when the sample is loaded into the diamond anvil cell for HP experiments. The pressure dependence of modes is linear with pressure in the three phases. Tables S3−S5 summarize the frequencies at various pressures and pressure coefficients. Noticeably, there are many phonons that gradually soften under compression in the low-pressure phase. This suggests that pressure tends to develop dynamical instabilities, which is consistent with the existence of a phase transition near ∼4 GPa. From Figure 11 the changes in the Raman frequencies and pressure coefficients become more evident. There is no doubt we have two phase transitions: one at ∼4 GPa and the other at ∼10.4 GPa.

In order to make a tentative mode assignment of Raman modes of the HP phases, we used DFT calculations. The

https://doi.org/10.1021/acs.jpcc.1c10483
J. Phys. Chem. C 2022, 126, 4664−4676

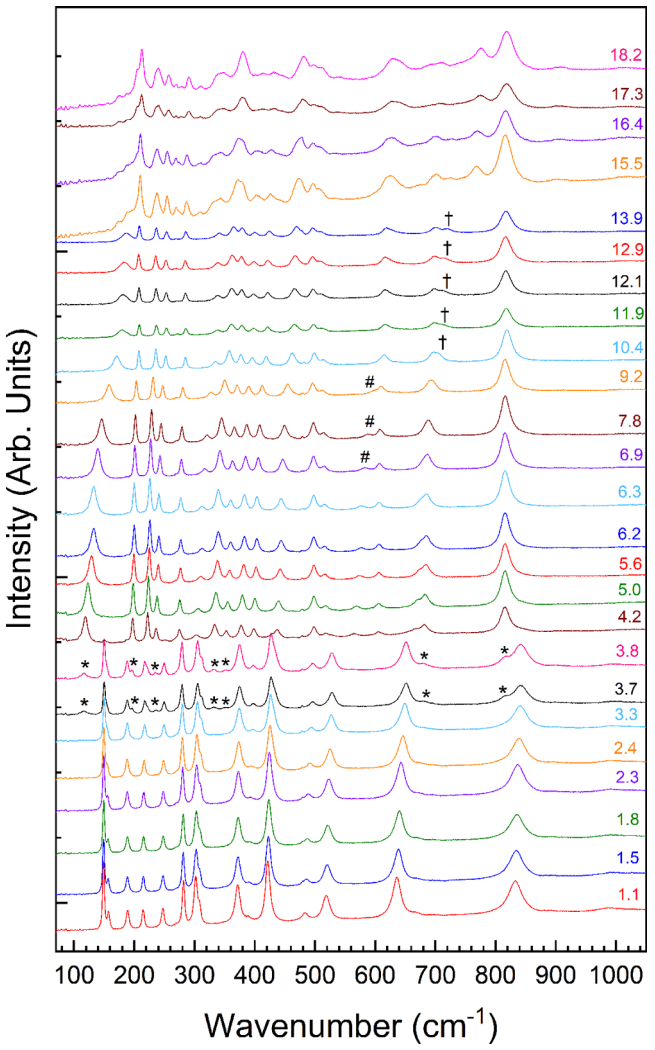

Figure 10. Selection of Raman spectra measured at different pressures (in GPa). Asterisks (∗) depict emerging peaks of phase HP1, pound signs (#) indicate disappearing peaks of phase HP1, and dagger symbols (†) highlight emerging peaks of phase HP2.

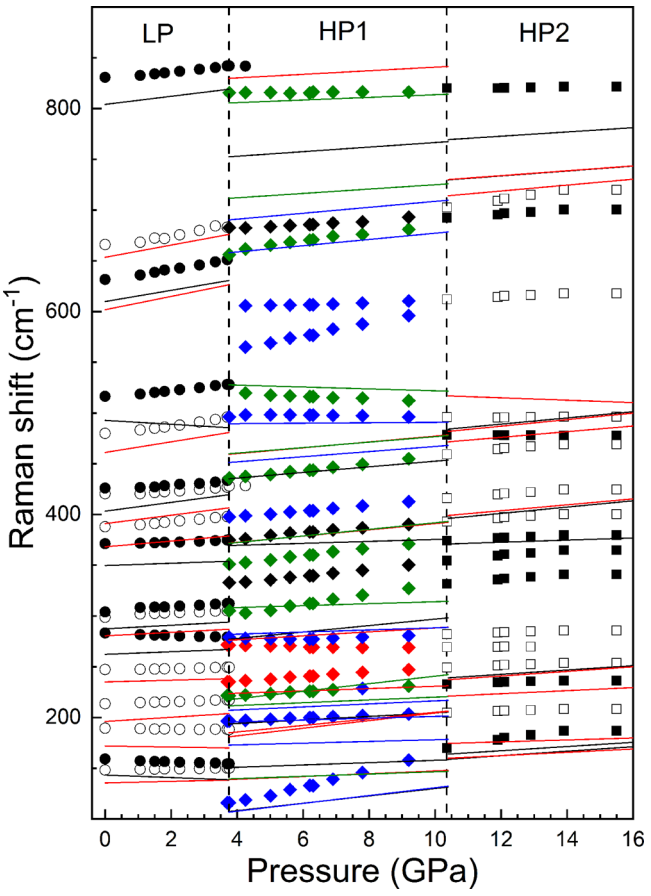

Figure 11. Pressure dependence of Raman modes. Different symbols are used for each phase. In phases LP and HP2, filled symbols are A_g modes and empty symbols are B_g modes. For phase HP1 we used black, red, blue, and green for A_g, B_{1g}, B_{2g}, and B_{3g}, respectively. Lines are results from DFT calculations. In phases LP and HP2, black lines are A_g modes and red lines are B_g modes. For phase HP1 the same code color as for symbols is used. Vertical dashed lines indicate transition pressures.

calculated pressure dependence of Raman modes is reported in Figure 11. In Tables S3−S5, we compare calculations with experiments. For the LP phase, the agreement is good regarding frequencies and pressure coefficients ($\frac{d\omega}{dp}$). In phases HP1 and HP2, the agreement is not as good as for the LP phase, but a correlation analysis[13] allows us to propose a mode assignment (see Tables S3−S5). HP2 sharing a space group and the number of atoms per unit cell with wolframite has also 18 Raman modes with A_g and B_g symmetry. The mechanical representation for phase HP1 is $\Gamma = 8A_g + 8A_u + 9B_{1g} + 9B_{1u} + 10B_{2g} + 10B_{2u} + 9B_{3g} + 9B_{3u}$. One B_{1u}, one B_{2u}, and one B_{3u} are the acoustic modes. The Raman modes are $8A_g$, $9B_{1g}$, $10B_{2g}$, and $9B_{3g}$. However, there are modes that are nearly degenerated; see Table S4. This, and a possible small Raman scattering cross section of some modes, could explain why only 19 modes are detected in experiments for phase HP1. For completeness, we have also calculated the pressure dependence of IR modes for all phases, which are reported in Tables S6 and S7. Noticeably in the LP phase, there are multiple IR-active modes that have negative pressure coefficients, confirming the tendency of wolframite $ScNbO_4$ to develop dynamical instabilities.

To close the work we will discuss the influence of pressure in the electronic band gap. We have performed DFT calculations and experimental measurements to provide information on the evolution of the band gap as a function of pressure. The optical absorption measurements and HSE06 results are shown in Figure 12. The plot related to the HSE06 band structure of HP1 is also gathered in Figure S2. In the LP phase, the band gap evolution with pressure is very weak. The behavior is indeed very similar to that of isomorphic $InNbO_4$.[13] The pressure coefficient of the band gap energy (dE_{gap}/dp) is 10 meV/GPa. This is mainly due to the incompressible nature of the structure and to the fact that states near the Fermi level are dominated by Nb 4d and O 2p states.[56] Furthermore, the bonding nature does not change significantly. The ionic index calculated using the QTAIM procedure shows that, in the low-pressure phase, the ionicity is 61% at ambient conditions, increasing up to 61.2% at the transition pressure. The phase transition enhances slightly the ionicity to 63.5%, increasing this parameter under compression until it reaches the value of 63.7% at 11 GPa (the pressure of the second transition). We have also found that the transition from wolframite to HP1 causes a abrupt decrease of the band gap value of about 1.8 eV.

https://doi.org/10.1021/acs.jpcc.1c10483
J. Phys. Chem. C 2022, 126, 4664−4676

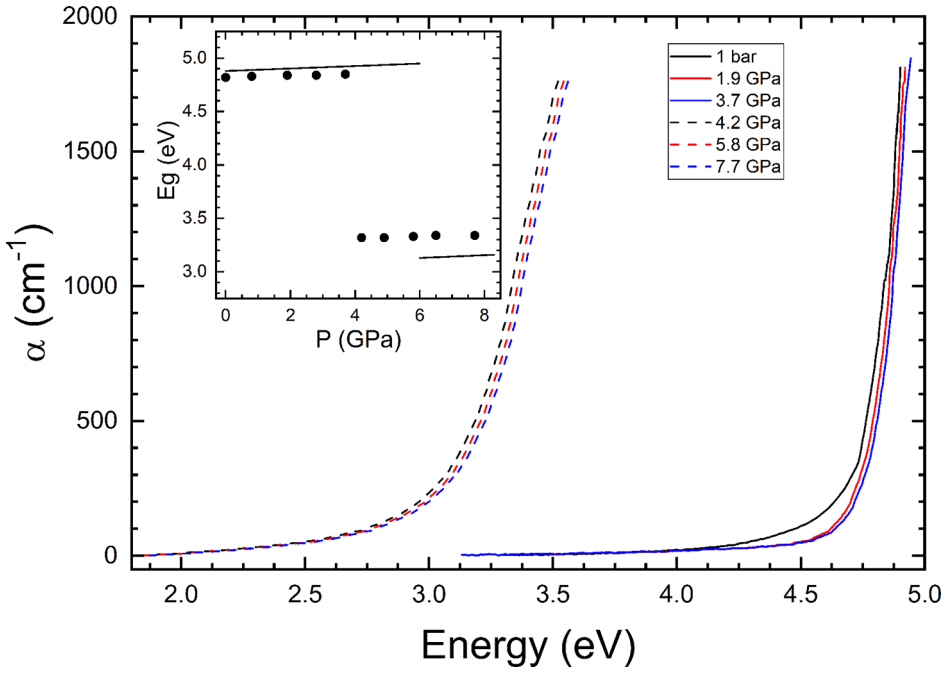

Figure 12. Optical absorption of $ScNbO_4$ at different pressures (indicated in the figure). The inset shows the pressure dependence of the band gap energy. Symbols are from experiments, and lines are from calculations.

Further, this structural transition also induces a change in the nature of the band gap. The HP1 structure presents an indirect band gap. In the HP1 phase, the indirect band gap is located at the X−U point. Again, in phase HP1, the band gap energy is little affected by pressure. Unfortunately, we could not perform optical absorption measurements in phase HP2 because, after the two-phase transition, the optical quality of the sample deteriorated, precluding the performance of accurate measurements. Therefore, we leave the characterization of the optical properties of phase HP2 to a future work.

CONCLUSIONS

We have reported an accurate characterization of the properties of $ScNbO_4$ at ambient pressure and under high pressure up to 18 GPa. We have found that wolframite-type $ScNbO_4$ is a direct band gap material with a band gap energy of 4.88 eV. We have determined the elastic constants and moduli and measured and assigned the 18 Raman-active modes. In addition, on the basis of density functional theory calculations, we have proposed the existence of two phase transitions at ∼5 and ∼11 GPa. We report the calculated crystal structures of the high-pressure phases, the compressibility of each phase, and the corresponding equations of state. The occurrence of the predicted phase transitions has been confirmed by high-pressure Raman and optical absorption measurements. These experiments provide information on the pressure evolution of phonon frequencies and the band gap energy. These results have been analyzed in the light of density functional theory calculations. Interestingly, the phase transition at ∼5 GPa induces a large collapse of the volume of the crystal structure and a large decrease of the band gap energy, which changes across the ultraviolet range at the first pressure-driven transition.

ASSOCIATED CONTENT

Supporting Information

The Supporting Information is available free of charge at https://pubs.acs.org/doi/10.1021/acs.jpcc.1c10483.

Additional information on ELF calculations; calculated Raman and IR modes for different phases; directional compressibility, band structure, ELF, Raman spectra measured after decompression (PDF)

AUTHOR INFORMATION

Corresponding Authors

Tarik Ouahrani − *Laboratoire de Physique Théorique, Université de Tlemcen, 13000 Tlemcen, Algeria; Ecole Supérieures en Sciences Appliquées, 13000 Tlemcen, Algeria*; Email: tarik.ouahrani@univ-tlemcen.dz

Daniel Errandonea − *Departamento de Física Aplicada, Instituto de Ciencia de Materiales, Matter at High Pressure (MALTA) Consolider Team, Universidad de Valencia, Burjassot E46100 Valencia, Spain*; orcid.org/0000-0003-0189-4221; Email: daniel.errandonea@uv.es

Authors

Alka B. Garg − *High Pressure and Synchrotron Radiation Physics Division and Process Development Division, Bhabha Atomic Research Centre, Mumbai 400085 Maharashtra, India*; orcid.org/0000-0003-4050-8469

Rekha Rao − *Solid State Physics Division, Bhabha Atomic Reserach Centre, Mumbai 400085 Maharashtra, India*; orcid.org/0000-0002-1848-6171

Placida Rodríguez-Hernández − *Departamento de Física, MALTA-Consolider Team, Instituto de Materiales y Nanotecnología, Universidad de La Laguna, San Cristóbal de La Laguna E38200 Tenerife, Spain*; orcid.org/0000-0002-4148-6516

Alfonso Muñoz − *Departamento de Física, MALTA-Consolider Team, Instituto de Materiales y Nanotecnología,*

https://doi.org/10.1021/acs.jpcc.1c10483
J. Phys. Chem. C 2022, 126, 4664−4676

Universidad de La Laguna, San Cristóbal de La Laguna E38200 Tenerife, Spain; orcid.org/0000-0003-3347-6518

Michael Badawi − *Université de Lorraine, LPCT, UMR 7019, F54506 Vandoeuvre-lès-Nancy, France;* orcid.org/0000-0002-3504-4180

Complete contact information is available at: https://pubs.acs.org/10.1021/acs.jpcc.1c10483

Author Contributions

T.O. contributed to conceptualization, DFT calculations, analysis, writing, and editing; A.B.G. contributed to synthesis, XRD, analysis, writing, and editing; R.R. contributed to Raman experiments; P.R.-H. and A.M. contributed to DFT calculations, analysis, writing, and editing; M.B. contributed to DFT calculations; and D.E. contributed to conceptualization, optical absorption, analysis, writing, and editing.

Notes

The authors declare no competing financial interest.

■ ACKNOWLEDGMENTS

D.E., A.M., and P.R.-H. acknowledge financial support given by the Spanish Research Agency (AEI) and Spanish Ministry of Science and Investigation (MCIN) under projects PID2019-106383GB-C41/C43/ (DOI: 10.13039/501100011033) and RED2018-102612-T (MALTA Consolider-Team Network). D.E. acknowledges financial support given by Generalitat Valenciana under Grant Prometeo/2018/123 (EFIMAT). We would like to thank TGCC under the allocation 2020-A0080910433 made by GENCI, the PMMS (Pôle Messin de Modélisation et de Simulation), the Tirant supercomputer (Universitat de Valencia), and the MALTA-Consolider facilities for providing us the computational resources.

■ REFERENCES

(1) Errandonea, D.; Manjon, F. J. Pressure effects on the structural and electronicproperties of ABX_4 scintillating crystals. *Prog. Mater. Sci.* **2008**, *53*, 711−773.

(2) Errandonea, D.; Garg, A. B. Recent progress on the characterization of the high-pressure behaviour of AVO_4 orthovanadates. *Prog. Mater. Sci.* **2018**, *97*, 123−169.

(3) Injac, S.; Yuen, A. K. L.; Avdeev, M.; Wang, C.-H.; Turner, P.; Brand, H. E. A.; Kennedy, B. J. Structural and magnetic studies of ABO_4-type ruthenium and osmium oxides. *Inorg. Chem.* **2020**, *59*, 2791−2802.

(4) Afif, A.; Zaini, J.; Rahman, S. M. H.; Eriksson, S.; Islam, M. A.; Azad, A. K. Scheelite type $Sr_{1-x}Ba_xWO_4$ (x = 0.1, 0.2, 0.3) for possible application in Solid Oxide Fuel Cell electrolytes. *Sci. Rep.* **2019**, *9*, 9173.

(5) Errandonea, D.; Ruiz-Fuertes, J. A brief review of the effects of pressure on Wolframite-Type Oxides. *Cryst.* **2018**, *8*, 71.

(6) Macavei, J.; Schulz, H. The crystal structureof wolframite type tungstates at high pressure. *Z. Kristallogr.* **1993**, *207*, 193−208.

(7) Hellenbrandt, M. The Inorganic Crystal Structure Database (ICSD)—Present and Future. *Crystallogr. Rev.* **2004**, *10*, 17−22.

(8) Zou, Z.; Ye, J.; Arakawa, H. Structural properties of $InNbO_4$ and $InTaO_4$: correlation with photocatalytic and photophysical properties. *Chem. Phys. Lett.* **2000**, *332*, 271−277.

(9) Keller, C. über ternäre Oxide des Niobs und Tantals vom Typ ABO_4. *Z. Anorg. Allg. Chem.* **1962**, *318*, 89−106.

(10) Botella, P.; Lopez-Moreno, P.; Errandonea, D.; Manjon, F. J.; Sans, J. A.; Vie, D.; Vomiero, A. High-pressure characterization of multifunctional $CrVO_4$. *J. Phys.: Condens. Matter* **2020**, *32*, 385403.

(11) Sun, H.; Yu, C.; Zheng, L.; Yang, F.; Mao, Q.; Ding, S. Experimental and theoretical investigations of the electronic structureand luminescent properties of undoped and rare-earth-doped $ScNbO_4$. *J. Mater. Sci.: Mater. Electron.* **2020**, *31*, 10260−10266.

(12) Lykova, I.; Rowe, R.; Poirier, G.; McDonald, A. M.; Giester, G. Nioboheftetjernite, $ScNbO_4$, a new mineral from the Befanamo Pegmatite, Madagascar. *Canad Mineral* **2021**, *59*, 445−452.

(13) Garg, A. B.; Errandonea, D.; Popescu, C.; Martinez-García, D.; Pellicer-Porres, J.; Rodríguez-Hernández, P.; Muñoz, A.; Botella, P.; Cuenca-Gotor, V. P.; Sans, J. A. Pressure-Driven Isostructural Phase Transition in $InNbO_4$: In Situ Experimental and Theoretical Investigations. *Inorg. Chem.* **2017**, *56*, 5420−5430.

(14) Ruiz-Fuertes, J.; Friedrich, A.; Errandonea, D.; Segura, A.; Morgenroth, W.; Rodríguez-Hernández, P.; Muñoz, A.; Meng, Y. Optical and structural study of the pressure-induced phase transition of $CdWO_4$. *Phys. Rev. B* **2017**, *95*, 174105.

(15) Errandonea, D. High pressure crystal structures of orthovanadates and their properties. *J. Appl. Phys.* **2020**, *128*, 040903.

(16) Söderlind, P.; Young, D. A. Assessing Density-Functional Theory for Equation-Of-State. *Comput.* **2018**, *6*, 13−26.

(17) Bader, R. F. W. *Atoms in Molecules: A Quantum Theory*; Clarendon Press: Oxford, U.K., 1990.

(18) Siqueira, K. P. F.; Moreira, R. L.; Dias, A. Synthesis and Crystal Structure of Lanthanide Orthoniobates Studied by Vibrational Spectroscopy. *Chem. Mater.* **2010**, *22*, 2668−2674.

(19) Segura, A.; Sans, J. A.; Errandonea, D.; Martinez-García, D.; Fages, V. High conductivity of Ga-doped rock-salt ZnO under pressure: Hint on deep-ultraviolet-transparent conducting oxides. *Appl. Phys. Lett.* **2006**, *88*, 011910.

(20) Mao, H. K.; Bell, P. M. High-Pressure Physics: The 1-Megabar Mark on the Ruby R_1 Static Pressure Scale. *Science* **1976**, *191*, 851−852.

(21) Kresse, G.; Furthmüller, J. Efficiency of ab-initio total energy calculations for metals and semiconductors using a plane-wave basis set. *Comput. Mater. Sci.* **1996**, *6*, 15−50.

(22) Kresse, G.; Hafner, J. Ab initio molecular dynamics for liquid metals. *Phys. Rev. B* **1993**, *47*, 558−561.

(23) Kresse, G.; Joubert, D. From ultrasoft pseudopotentials to the projector augmented-wave method. *Phys. Rev. B* **1999**, *59*, 1758−1775.

(24) Perdew, J. P.; Ruzsinszky, A.; Csonka, G. I.; Vydrov, O. A.; Scuseria, G. E.; Constantin, L. A.; Zhou, X.; Burke, K. Restoring the Density-Gradient Expansion for Exchange in Solids and Surfaces. *Phys. Rev. Lett.* **2008**, *100*, 136406.

(25) Heyd, J.; Scuseria, G. E.; Ernzerhof, M. Hybrid functionals based on a screened Coulomb potential. *J. Chem. Phys.* **2003**, *118*, 8207−8215.

(26) Togo, A.; Tanaka, I. First principles phonon calculations in materials science. *Scr. Mater.* **2015**, *108*, 1−5.

(27) Gonze, X.; Lee, C. Dynamical matrices, Born effective charges, dielectric permittivity tensors, and interatomic force constants from density-functional perturbation theory. *Phys. Rev. B* **1997**, *55*, 10355−10368.

(28) Nielsen, O. H.; Martin, R. M. Quantum-Mechanical Theory ofStress and Force. *Phys. Rev. B: Condens. Matter Mater. Phys.* **1985**, *32*, 3780−3791.

(29) Boto, R. A.; Piquemal, J. P.; Contreras-García, J. Revealing strong interactions with the reduced density gradient: a benchmark for covalent, ionic and charge-shift bonds. *Theor. Chem. Acc.* **2017**, *136*, 139.

(30) Johnson, E. R.; Keinan, S.; Mori-Sanchez, P.; Contreras-García, J.; Cohen, A. J.; Yang, W. Revealing noncovalent interactions. *J. Am. Chem. Soc.* **2010**, *132*, 6498−6506.

(31) Brixner, L. H. On the structural and luminescent properties of the $ScTa_{1-x}Nb_xO_4$ system. *J. Chem. Educ.* **1980**, *57*, 588−5909.

(32) Csonka, G. I.; Perdew, J. P.; Ruzsinszky, A.; Philipsen, P. H. T.; Lebègue, S.; Paier, J.; Vydrov, O. A.; Ángyán, J. G. Assessing the performance of recent density functionals for bulk solids. *Phys. Rev. B* **2009**, *79*, 155107.

(33) Birch, F. Finite Strain Isotherm and Velocities for Single-Crystaland Polycrystalline NaCl at High Pressures and 300 K. *J. Geophys. Res.* **1978**, *83*, 1257−1268.
(34) Hazen, R. M.; Finger, L. W. Bulk modulus. volume relationshio for cation-anion polyhedra. *J. Geophys. Res.* **1979**, *84*, 6723−6728.
(35) Bandiello, E.; Rodríguez-Hernández, P.; Muñoz, A.; Buenestado, M. B.; Popescu, C.; Errandonea, D. Electronic properties and high-pressure behavior of wolframite-type $CoWO_4$. *Mater. Adv.* **2021**, *2*, 5955−5966.
(36) Ougherb, C.; Ouahrani, T.; Ferouani, A. K. Untangling electronic, elastic and bonding properties of the $ThGeO_4$ host material from first principles calculation. *Eur. Phys. J. B* **2017**, *90*, 146.
(37) Born, M.; Huang, K. *Dynamical Theory of Crystal Lattices*; Oxford University Press: Oxford, U.K., 1954.
(38) Errandonea, D.; Muñoz, A.; Gonzalez-Platas, J. Comment on "High-pressure x-ray diffraction study of YBO_3/Eu^{3+}, $GdBO_3$, and $EuBO_3$: Pressure-induced amorphization in $GdBO_3$" [J. Appl. Phys. 115, 043507 (2014)]. *J. Appl. Phys.* **2014**, *115*, 216101.
(39) Ouahrani, T.; Öztekin Çiftci, Y.; Mebrouki, M. Dynamical and anisotropic behavior of the $MSiP_2$ (M= Be, Mg, Cd, Zn and Hg) compounds. *J. Alloys Compd.* **2014**, *610*, 372−381.
(40) Gaillac, R.; Pullumbi, P.; Coudert, F.-X. ELATE: an open-source online application for analysis and visualization of elastic tensors. *J. Phys.: Condens. Matter* **2016**, *28*, 275201−275206.
(41) Ruiz-Fuertes, J.; Errandonea, D.; Lopez-Moreno, S.; González, J.; Gomis, O.; Vilaplana, R.; Manjon, F. J.; Muñoz, A.; Rodriguez-Hernandez, P.; Friedrich, A.; et al. High-pressure Raman spectroscopy and lattice-dynamics calculations on scintillating $MgWO_4$: Comparison with isomorphic compounds. *Phys. Rev. B* **2011**, *83*, 214112.
(42) Blasse, G.; Dirksen, G. J.; Brixner, L. H. The influence of structural disorder on the luminescence of niobates: scandium niobate and magnesium niobate. *Mater. Chem. Phys.* **1986**, *14*, 485−494.
(43) Errandonea, D.; Muñoz, A.; Rodriguez-Hernandez, P.; Gomis, O.; Achary, S. N.; Popescu, C.; Patwe, S. G.; Tyagi, A. K. High-Pressure Crystal Structure, Lattice Vibrations, and Band Structure of $BiSbO_4$. *Inorg. Chem.* **2016**, *55*, 4958−4969.
(44) Ouahrani, T.; Medjdoub, F.-Z.; Gueddida, S.; Fernandez, Á. L.; Franco, R.; Benkhettou, N.-E.; Badawi, M.; Liang, A.; Gonzalez, J.; Errandonea, D. Understanding the Pressure Effect on the Elastic, Electronic, Vibrational, and Bonding Properties of the $CeScO_3$ Perovskite. *J. Phys. Chem. C* **2021**, *125*, 107−119.
(45) Kamencek, T.; Wieser, S.; Kojima, H.; Bedoya-Martinez, N.; Durholt, J. P.; Schmid, R.; Zojer, E. Evaluating Computational Shortcuts in Supercell-Based Phonon Calculations of Molecular Crystals: The Instructive Case of Naphthalene. *J. Chem. Theory Comput.* **2020**, *16*, 2716−2735.
(46) Lacomba-Perales, R.; Errandonea, D.; Martinez-Garcia, D.; Rodríguez-Hernández, P.; Radescu, S.; Mujica, A.; Muñoz, A.; Chervin, J. C.; Polian, A. Phase transitions in wolframite-type $CdWO_4$ at high pressure studied by Raman spectroscopy and density-functional theory. *Phys. Rev. B* **2009**, *79*, 094105.
(47) Ribeiro-Claro, P. J. A.; Vaz, P. D.; Nolasco, M. N.; Gil, F. P. S. C.; Batista de Carvalho, L. A. E.; Marques, M. P. M.; Amado, A. M. New Insights on the Vibrational Dynamics of 2-Methoxy-, 4-Methoxy- and 4-Ethoxy-Benzaldehyde from INS Spectra and Periodic DFT Calculations. *Materials* **2021**, *14*, 4561.
(48) Errandonea, D. High-pressure phase transitions and propertiesof MTO_4 compounds with the monazite-type structure. *Phys. Status Solidi B* **2017**, *254*, 1700016.
(49) Botella, P.; Enrichi, F.; Vomiero, A.; Muñoz-Santiuste, J. E.; Garg, A. B.; Arvind, A.; Manjon, F. J.; Segura, A.; Errandonea, D. Investigation on the Luminescence Properties of $InMO_4$ (M = V^{5+}, Nb^{5+}, Ta^{5+} Crystals Doped with Tb^{3+} or Yb^{3+} Rare Earth Ions. *ACS OmegaB* **2020**, *5*, 2148−2158.
(50) Ouahrani, T.; Merad-Boudia, I.; Baltache, H.; Khenata, R.; Bentalha, Z. Effect of pressure on the global and local properties of cubic perovskite crystals. *Phys. Scr.* **2011**, *84*, 025704−025711.
(51) Ouahrani, T.; Menendez, J. M.; Marqués, M.; Contreras-García, J.; Baonza, V. G.; Recio, J. M. Local pressures in Zn chalcogenide polymorphs. *Europhys. Lett.* **2012**, *98*, 56002−56008.
(52) Becke, A. D.; Edgecombe, K. E. A simple measure of electron localization in atomic and molecular systems. *J. Chem. Phys.* **1990**, *92*, 5397−5404.
(53) Tahri, K.; Ouahrani, T.; Pilmé, J. Understanding phase transition in the $ZnSiP_2$ chalcopyrite, a quantum chemical topology study. *Theor. Chem. Acc.* **2017**, *136*, 119.
(54) Errandonea, D.; Gomis, O.; Santamarıa-Perez, D.; García-Domene, B.; Muñoz, A.; Rodrıguez-Hernandez, P.; Achary, S. N.; Tyagi, A. K.; Popescu, C. Exploring the high-pressure behavior of the three known polymorphs of $BiPO_4$: Discovery of a new polymorph. *J. Appl. Phys.* **2015**, *117*, 105902.
(55) Klotz, S.; Chervin, J. C.; Munsch, P.; Le Marchand, G. Hydrostatic limits of 11 pressure transmitting media. *J. Phys. D: Appl. Phys.* **2009**, *42*, 075413.
(56) Ruiz-Fuertes, J.; Lopez-Moreno, S.; Lopez-Solano, J.; Errandonea, D.; Segura, A.; Lacomba-Perales, R.; Muñoz, A.; Radescu, S.; Rodriguez-Hernandez, P.; Gospodinov, M.; et al. Pressure effects on the electronic and optical properties of AWO_4 wolframites (A = Cd, Mg, Mn, and Zn): The distinctive behavior of multiferroic $MnWO_4$. *Phys. Rev. B* **2012**, *86*, 125202.

https://doi.org/10.1021/acs.jpcc.1c10483
J. Phys. Chem. C 2022, 126, 4664−4676